Transcranial 3D ultrasound localization microscopy using a large element matrix array with a multi-lens diffracting layer: an in vitro study

Hugues Favre, Mathieu Pernot, Mickael Tanter, Clément Papadacci

Transcranial 3D ultrasound localization microscopy using a large element matrix array with a multi-lens diffracting layer: an in vitro study

Hugues Favre[1], Mathieu Pernot[1], Mickael Tanter[1] and Clément Papadacci[1]

[1] Institute Physics for Medicine Paris, Inserm U1273, ESPCI Paris-PSL, Cnrs UMR8063, 75012 Paris, France

E-mail: clement.papadacci@espci.fr

Abstract

Objective
Early diagnosis and acute knowledge of cerebral disease require to map the microflows of the whole brain. Recently, ultrasound localization microscopy (ULM) was applied to map and quantify blood microflows in 2D in the brain of adult patients down to the micron scale. Whole brain 3D clinical ULM remains challenging due to the transcranial energy loss which reduces significantly the imaging sensitivity.
Approach
Large aperture probes with a large surface can increase both the field of view and sensitivity. However, a large active surface implies thousands of acoustic elements, which limits clinical translation. In a previous simulation study, we developed a new probe concept combining a limited number of elements and a large aperture. It is based on large elements, to increase sensitivity, and a multi-lens diffracting layer to improve the focusing quality. In this study, a 16 elements prototype, driven at 1MHz frequency, was made and in vitro experiments were performed to validate the imaging capabilities of this new probe concept.
Main results
First, pressure fields emitted from a large single transducer element without and with diverging lens were compared. Low directivity was measured for the large element with the diverging lens while maintaining high transmit pressure. The focusing quality of 4x3cm matrix arrays of 16 elements without/with lenses were compared. In vitro experiments in a water tank and through a human skull were achieved to localize and track microbubbles in tubes.
Significance
Ultrasound localization microscopy (ULM) was achieved demonstrating the strong potential of multi-lens diffracting layer to enable microcirculation assessment over a large field of view through the bones.

Keywords: ultrasound imaging, blood flow, super-resolution, 3D imaging, transducers, transcranial imaging, ultrasound localization microscopy

1. Introduction

The human vascular network is a complex multi-scale system ranging from several millimeters for the largest arteries to a few micrometers for the smallest vessels called capillaries. This network provides nutrition and dioxygen to organs and thus is linked to organs' functions and good health status. From a clinical point of view, assessing microcirculation morphological and functional abnormalities are essential to prevent the outbreak of a disease. For instance, cerebrovascular diseases are a common cause of death worldwide [1] and are mostly diagnosed at later stages after the apparition of acute symptoms. The early diagnosis of these diseases requires an efficient screening imaging system able to image the whole cerebral vascular network down to a micrometer scale. However, it remains a major challenge in clinical medical imaging.

Cerebral vasculature imaging is mainly performed via Computed Tomography scan and magnetic resonance angiography. However, these imaging technics require heavy and costly infrastructures, and are classically limited to a millimeter-scale resolution which could be not sufficient to image the smallest vessels involved in microcirculation dysfunction.

In the clinic, ultrasound imaging benefits from its portability, affordability, and its good spatio-temporal resolution to image blood flow dynamics at a millimeter scale resolution. However, clinical ultrasound still cannot assess the smallest vessels due to low spatial resolution.

In biomedical research, ultrasound imaging is an extremely active field and in the past decade, a new modality has emerged to enable microcirculation visualization. Inspired by optical localization microscopy (stochastic optical reconstruction microscopy (STORM), photoactivated localization microscopy (PALM), and fluorescence PALM), ultrasound localization microscopy (ULM) consists in imaging isolated microbubbles previously injected in the vascular system. The localization and the tracking of the center of these bubbles can be accumulated over time to create density and velocity maps of vascular networks . ULM spatial resolution goes beyond the fundamental ultrasound diffraction limit and can resolve micro vessels [2–5]. ULM was applied to reveal cerebral, tumoral, and kidney microflows on animal models ([5–7]) and recently on humans [8,9], with unprecedented resolution in the ultrasound field, down to a few micrometers.

In ULM methods, microbubbles are required to resolve the smallest vessels. They were originally used in clinical practice to enhance echogenicity of the largest vessels in the patient brain to detect abnormalities. However, even with the use of microbubbles imaging through the human skull remains challenging because ultrasonic waves suffer from reflections, absorbtion and aberrations when travelling through the skull.

In a recent clinical proof-of-concept study [8], 2D transcranial ULM was shown feasible to map the vascular network and blood-flow dynamics at high spatial resolution to detect aneurysm in patients. This study opened new perspectives in cerebrovascular pathologies screening and diagnostics. Still, two-dimensional imaging is operator-dependent, and the risk to miss out-of-planes features during examinations is important. To be fully translated to clinical practice, 3D ULM over the whole brain must be developped.

The feasibility of 3D ULM with matrix probes was made possible through the development of 3D programmable ultrafast scanners with approximately 1 thousand channels in transmit and receive [10,11]. Small aperture matrix probes with 1024 fully connected elements were recently used to perform 3D ULM on rodents [12,13]. Translation to humans will require enlarging these matrix probes to reach high sensitivity, good focusing quality and a large field of view. However, increasing the number of channels to drive large matrix arrays is a technical challenge associated with tremendous cost and cumbersomeness. Different types of ultrasonic probes: multiple linear probes [14], multiplexed 2D matrix arrays [15,16], rowcolum addressed (RCA) arrays [17], sparse 2D arrays [18] and hemi-spherical array [19] were developed and used in vitro and in vivo demonstrating promising results while reducing the number of elements and channels. However, these approaches could have a limited impact for transcranial ULM, mainly due to a limited sensitivity or a small field of view.

Classical sparse 2D arrays use a low number of small elements sparsly distributed over the probe surface which limits the transmit acoustic energy and receive sensitivity. Sparse methods using large transducers can increase the element sensitivity and was proposed in the photoacoustic field where the received signals are particularly weak. To overcome the directivity issues and enable focusing in receive, diverging acoustic lenses were added to the transducer surface [20]. A multi-lens array was made and beamforming in receive was performed for photoacoustic application [21]. Recently, we introduced the concept of multi-lens arrays in the ultrafast ultrasound imaging field. Simulation study demonstrated the strong potential to use this approach for 3D ULM over a large field of view through the bones with a reduced number of transducers [22]. In this previous study, the multi-lens array was modelled as an array of 256 curved elements over a surface of 10x10cm² and was able to image a large volume of 10x10x10cm³ in a transcranial setting.

In this study, we propose to validate experimentally the imaging capabilities of a multi-lens probe for large field transcranial 3D ULM application using an array of diverging lenses placed in front of large transducers. A 4x4 element matrix array prototype was developed and acoustic diverging lenses were built. The acoustic properties of large transducers

without and with the lenses were compared. A single element study and a focusing study were performed. In vitro experiments in a water tank and through a human skull were achieved to localize and track microbubbles in tubes and to demonstrate the feasability of 3D ULM with a large element matrix array combined with diverging lenses.

2. Materials and methods

2.1 Matrix array design and construction

2.1.1 Experimental approach

A matrix probe prototype of 16 transducers (4x4 circular elements, 7mm diameter, 950kHz central frequency, 50% bandwidth at -6dB, Imasonic, France) was made, figure 1a-b) . The matrix probe was driven at a central frequency of 1Mhz to limit the attenuation coefficient of the wave when travelling through the skull bone (10dB/cm) [23]. A matrix of large tranducers with diverging lens was made by adding a multi lens diffracting layer on the front of the original matrix. In transmit, 1 cycle at a central frequency of 1MHz was set with a 0.67 duty cycle and a transmit power controller (TPC) maximum high voltage of 70V. For the different configurations, the same transmit sequences were set.

Maximal pressure maps were measured experimentally for individual transducers to assess transmit pressure and directivity. Focusing performances and point spread function were also compared. Finally, the matrix with the multi lens diffracting layer was used to perform 3D ULM.

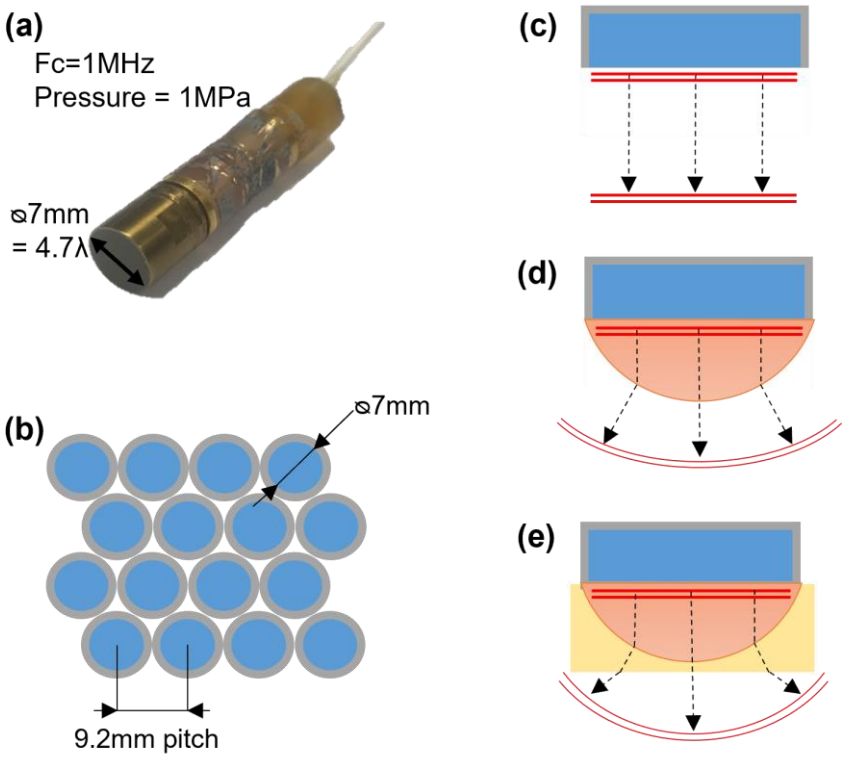

Figure 1. Matrix arrays design. (a) photo of one piezoelectric transducer used in the matrix configurations. (b) Schema of the element distribution in the matrix array. Schematics of emitted ultrasound waves by: a large element (c), a large element with simple lens (d), a large element with compound lens (e). Double red lines represent the wave front, black doted arrows shows the ray tracing, orange hemi-sphere represent the lens, and yellow rectangle represents the filler material of the compound lens.

2.1.2 Matrix array prototype construction

A 16-element matrix array was made from individual transducers and assembled thanks to 3D printed parts. The transducers were distributed in a hexagonal pattern to maximize the compactness, as shown in figure 1, with an inter-element pitch of 9.2mm. The probe aperture in the lateral dimension was 41.4mm by 30.8mm, and an active surface of 616mm². The transducers were connected, with an electrical impedance matching, to a Vantage ultrasound device (Verasonics, Kirkland, USA).

2.1.3 Multi diffracting layer construction

The multi diffracting layer was made of hemispherical lenses of 8mm diameter placed on a 0.5mm thickness plate. A mold of silicone was made and the layer of lenses was cast in Stycast 1090SI Epoxy (Henkel Loctite).

To increase the diverging effect of the acoustic lens, a supplementary layer was added on top of the stycast lenses. The combined 2 parts are called compound lens [24], i.e. figure 1 (e). The additional layer, made of silicone (Elite Double 8, ZHERMACK) was cast directly on the epoxy lenses.

2.2 Pressure Field characterization of single elements

The matrix array was imerged in a water tank and the pressure field was measured with a broadband needle hydrophone (HNC0400, Onda). One transducer was selected to emit the ultrasonic wave, and the corresponding pressure field characterization was done identically for the 3 configurations (large element without lens, large element with lens, large element with coumpound lens). 2D scans were done in the axial plane of the emitter with a 1.5mm step. The maximal value over time was taken and linear interpolation was done to increase the spatial sample rate by 10. Maximal pressure amplitudes at 4cm depth on the axial axis and on the side (30° off-axis) were compared. The amplitude profile along a circular arc of 30mm radius was computed and the directivity of the elements was quantified as the angle defined by a 6dB pressure drop.

2.3 Matrix array comparison

2.3.1 Focusing characterization

The focusing performances of the matrix arrays were assessed by measuring the maximal pressure fields of a focused transmit. Pressure fields were acquired with the same experimental setup described in session 2.2. The maximal pressure was measured in two planes: axial and lateral, with a half wavelength (0.75mm) step. Maximal pressure at the focus spot and the full width at half maximum were assessed.

2.3.2 3D ultrafast imaging

Ultrafast imaging was performed at a pulse repetition frequency (PRF) of 6.7kHz using 16 diverging waves with the virtual sources placed at the transducer location [25,26] emitted successively with a resulting volume rate of 417 images/s. In receive, dynamic focusing was performed in each voxel with a constant ‘f over d’ value of 1 (where ‘f’ is depth and ‘d’ the aperture size).

Backscattered radio-frequency (RF) signals were acquired with a sampling frequency of 4MHz and stored in memory. The RF signals of each element were processed using a 3D delay and sum algorithm as it is done in [11]. Coherent compounding was performed by coherently summing the 16 images.

For the large element array, classical focusing delay law was applied by computing the time delay (τ) corresponding to the Euclidian distance between the center of the transducer C and the focal point F. For the large element array with lenses, a corrected delay law was applied. This correction takes into account the propagation in the lens of radius R (whose speed of sound c_{lens}, differs from water c_{water}), from the center of the transducer to the focal point (Eq1).

$$\tau_{lens\_correction} = \frac{dist(C,F) - R}{c_{water}} + \frac{R}{c_{lens}} \quad (1)$$

2.3.3 Point spread function

A tip of a metallic needle of a diameter smaller than half wavelength placed at 4cm depth was imaged with the large element array without and with lens. The 3D images also called the point spread function (PSF) were normalized by their maximum and log compression was applied. 3D images are displayed in 3D via the software Amira (Thermo Fisher Scientific). The projection of the maximum value on the lateral plane was displayed as well as the orthogonal projection of the maximum values on the first lateral axis.

2.4 Ultrasound localization microscopy in free space

2.4.1 Tube phantom

A silicone tube was imaged in water with the large element matrix array with diffracting layer described in session 2.1. The inner diameter of the tube given by the manufacturer is 1.5mm. A flow rate of 6.7mL/min was imposed. The perfused solution was composed of Sonovue microbubble solution, 1:500 (vol) diluted in water. The water used in the dilution of the Sonovue solution was previously degassed for more than 15min in a vacuum bell at 3 mbar. The tube was twisted, forming a double helix with opposite flow directions. The tube was positioned between 3 to 6cm depth in front of the probe.

3D Ultrafast imaging was performed at a volume rate of 417 images/s (ie. one transmit every 150µs). Acquisitions of the RF signals were made by blocs of 1024 frames, corresponding to 2.5 seconds of acquisition per bloc. RF signals were directly saved in an SSD disk for about 7s. 14 blocs were acquired corresponding to 34s acquisition. The RF signals were stored and the beamforming was done afterward. RF data were beamformed on a 3D volume of from 3cm to 7cm depth and from -2cm to 2cm in both lateral axes. The volume was divided into voxels of 0.75x0.75x0.75mm size. The beamforming was performed using Matlab software, on a graphic processing unit (Nvidia RTX A6000). It took 5.12 s to beamform 1024 frames.

Once the RF signals were acquired and beamformed a preprocessing singular value decomposition (SVD) filtering [27] was applied. The SVD was done on blocs of 512 frames, the first 3 singular values were removed, to filter the static signal from the reflection of the tube. The 14 336 images were used to generate a 3D power doppler of the tube, as well as a density map, and a velocity map of the tube thanks to a ULM algorithm (see next session 2.4.2).

2.4.2 Localization and tracking

After SVD filtering, bubble detection was performed using a standard ultrasound localization microscopy (ULM) algorithm [13,15]. Local maxima were detected in the image. Only local maxima above -6dB were kept. Then for each local maxima, a correlation with a gaussian point-spread-function was performed and the positions whose correlation coefficient was above 0.6 were considered microbubbles. A 3D paraboloid interpolation of the center of the bubble was computed. Finally, a tracking algorithm was applied. The algorithm matched the positions of bubbles between successive frames with a maximum velocity of 200mm/s. Only the positions tracked over at least 3 frames were kept. After bubble localization and tracking, bubble positions in all the frames were stacked in the imaging space divided in voxel of 150x150x150µm³ to create a density map. In the same way, a velocity map was created by averaging bubble velocities in each voxel.

The mean velocity and the corresponding standart devation (std) were assessed. The inner diameter of the tube was measured on 10 orthogonal cross-sections of the density map as the width at one-fifth of the maximum (density = 0.2). Mean and standard deviation were performed.

A slice of the velocity map perpendicular to the helix axis, of 1.5mm thickness was assessed. The velocities were average along the thickness dimension. A velocity profile was determined.

2.5 Transcranial imaging

2.5.1 Transcranial PSF, and aberration correction

An adult human skull cut transversally was degassed in water for 48h to remove entrapped air in bone cavities. The skull was carefully kept in water during the entire experiment. The 16-element probe with the diverging lenses was positioned next to the outer temporal area.

The tip was imaged, following the ultrafast imaging method described in session 2.3.2. The 3D image represents a transcranial PSF. RF acquired and processed were also used to generate a transcranial PSF with aberration correction. The algorithm used was adapted from the one previously described in [8]. The uncorrected transcranial PSF was used to determine the location of the metallic tip thanks to a 3D paraboloid interpolation. The delay laws were computed for this very location (see Eq4), as a theoretical reference for the aberration correction.

To determine the delay laws describing the skull aberrations, a synthetic temporal response was computed according to the element characteristics used: a pulse of centrale frequency 1MHz and 50% bandwidth at -6dB. A cross-correlation was computed between the synthetic temporal response and the RF. The maxima of the cross-correlation were used to determine the aberrated delays laws for each transmit-receive echos, reflected at the location of the tip. The aberrated delay laws were subtracted from the theoretical delay laws (Eq 4) to find the aberration correction. Isoplanatism approximation was assumed in the whole image volume, and the aberration correction computed was applied to beamformed a corrected 3D image, called the transcranial corrected PSF.

The two 3D PSF were compared and displayed in logarithmic compression. Grating lobes' level was assessed and signal to noise was measured as the mean of 25 voxels located at top corner of the imaging volume (away from grating lobes).

2.5.2 Transcranial ultrasound localization microscopy

The 16-element probe with the diverging lenses was positioned next to the outer temporal area of the human skull previously degassed. Three different in vitro experiments were carried out, with three different tubes. Two polyethylene tubes of 580 µm (± 80 µm) and 280 µm (± 28 µm) inner diameters were placed inside a human skull, as well as the twisted silicone tubes of 1.5mm inner diameter. The tubes were hooked up to a syringe to impose a flow rate of 1mL/min, 0.5ml/min and 6.7ml/min respectively. The perfused solutions in the tubes were composed of Sonovue microbubble solution, 1:100 (vol), 1:30 (vol) and 1:500 (vol) respectively diluted in degassed water for the three experiments. Ultrafast imaging was done (417Hz volume rate), and 32 blocs of 1024 volumes were acquired for the first experiment with the 580 µm diameter tube, and 24 blocs were acquired for the 280 µm and 1.5 mm diameter tubes. These acquisitions correspond respectively to 1 min 19s, and 59s of acquisition. RF data were beamformed. The same ULM method described the session 2.4.2 was used. The tracking algorithm was applied to match the bubbles' positions between successive frames with a maximum velocity of 200mm/s for the 580 um and 1.5mm diameter tube and 400mm/s for the 280 µm diameter tube . Density and velocity maps were generated on a 3D volume of 150x150x150µm³ voxels. The lateral projected length of the tubes were measured, on maximum projection on the longest lateral axis of the density map. The density profile cross section of the tube was averaged over a length of 0.3 mm.

The inner diameter of the tube was measured on orthogonal cross-sections of the density map as the width at one-fifth of the maximum (density = 0.2). Mean and standard deviation were performed.

3. Results

3.1 Single element pressure field

The acoustic field emitted by a large element, a large element with an acoustic lens and a large element with a compound lens are compared in figure 2. The pressure field from the large transducer of 4.7 λ diameter is collimated around the axial axis (figure 2 (a)). Figure 2 (b) shows that the directivity of the pressure field of the large transducer can be lowered by adding an acoustic lens, and even more when the compound lens is added, figure 2 (c). These qualitative observations were confirmed by the amplitude profiles assessed at a 30mm depth (figure 2(g)). The angular directivity at -6dB of the large element is 12°. When a simple lens or a compound lens is added in front of the large element, the angular directivity increases respectively to 30° and 40°.

Temporal response at 30mm depth and 10mm off-axis are displayed figure 2. For the large element without lens, the temporal signal is lengthened and the bandwidth is reduced (d). Large element with the stycast lens (e) presents clean temporal response and larger bandwidth. Compound lens signal is also lengthened due to impedance mismatch reflections in the compound lens.

Absolute pressures were measured on-axis (r=40mm, θ=0°) and off-axis (r=40mm, θ=30°). The pressure on-axis delivered by the large element was found to be 170 kPa. When simple lens or the compound lens was added in front of the large element the pressure drops respectively to 49kPa and 29kPa on-axis. However, the pressure delivered by the large element on the side was found to be 5.9kPa. For the simple and compound lens, we found an increase of 14kPa and 10kPa respectively. The quantitative results are gathered in table I.

TABLE I

TYPE OF ELEMENT	Pressure on-axis (kPa) (r=4cm, θ=0°)	Pressure off-axis (kPa) (r=4cm, θ=30°)	Directivity (°)
Large	170	5.9	12
Large + Stycast lens	49	14	30
Large + compound lens	29	10	40

Table1: Maximum pressure field at two locations on-axis and off-axis, and the angular aperture at -6dB of the different elements.

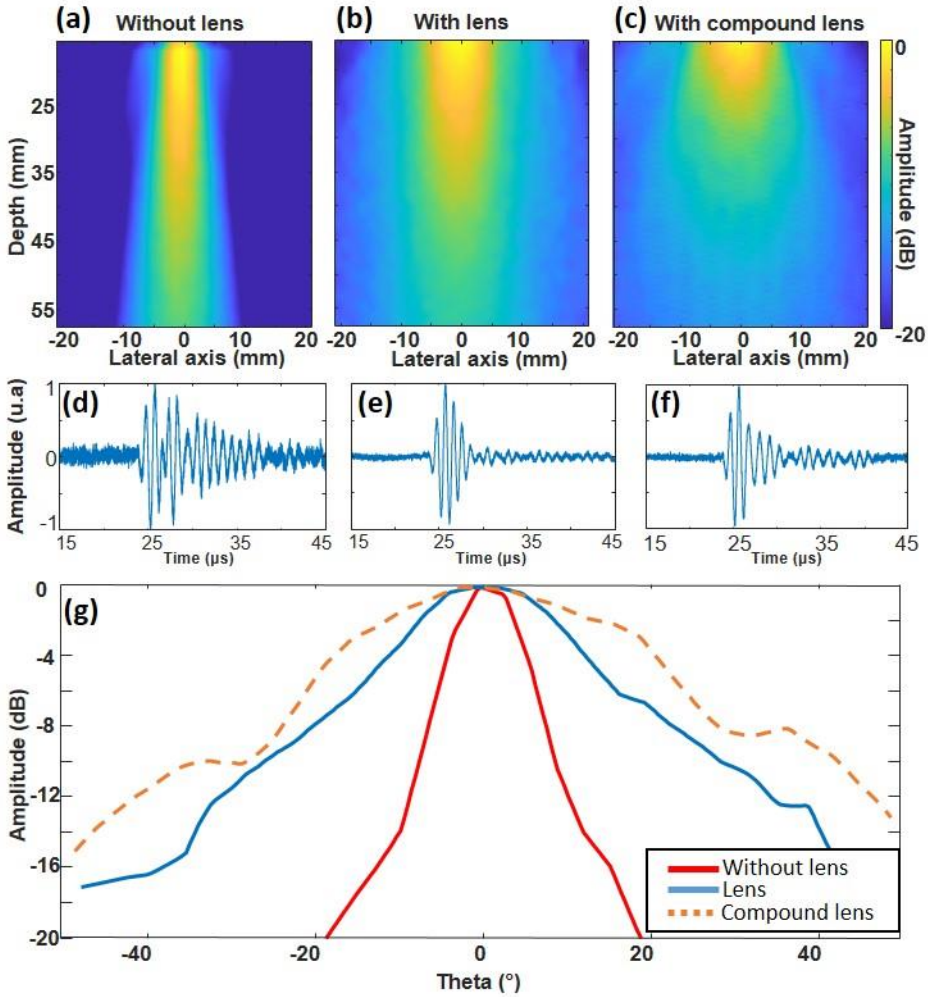

Figure 2. Single element pressure fields. (a) Maximum pressure field in the axial plane of a circular element of a 4λ diameter. Maximum pressure field in the axial plane of a circular element of 4λ diameter with a single lens made of Stycast (b) and with a compound lens (c). Temporal response measured at 3cm depth and 1cm off the axial axis of the large element (d), large element with a Stycast lens (e) and large element with a compound lens (f). Amplitude profile taken at 30 mm depth (g).

3.2 Matrix array comparisons: imaging performances

3.2.1 Focusing study

16-element Matrix arrays were made to compare the collective effect of large elements (figure 3a), and large elements with lens (figure 3 b). The imaging performances of these matrices were assessed by focusing at 4 cm depth. The corresponding maximal pressure field in the axial and lateral planes of the matrix arrays are displayed in figure 3 c-d). The matrix array composed of large elements without lens shows large grating lobes. These lobes were reduced using lenses. Width at half the maximum (-6dB) in the axial plane was respectively found to be 3.9mm, and 2.5mm showing a better resolution using lenses.

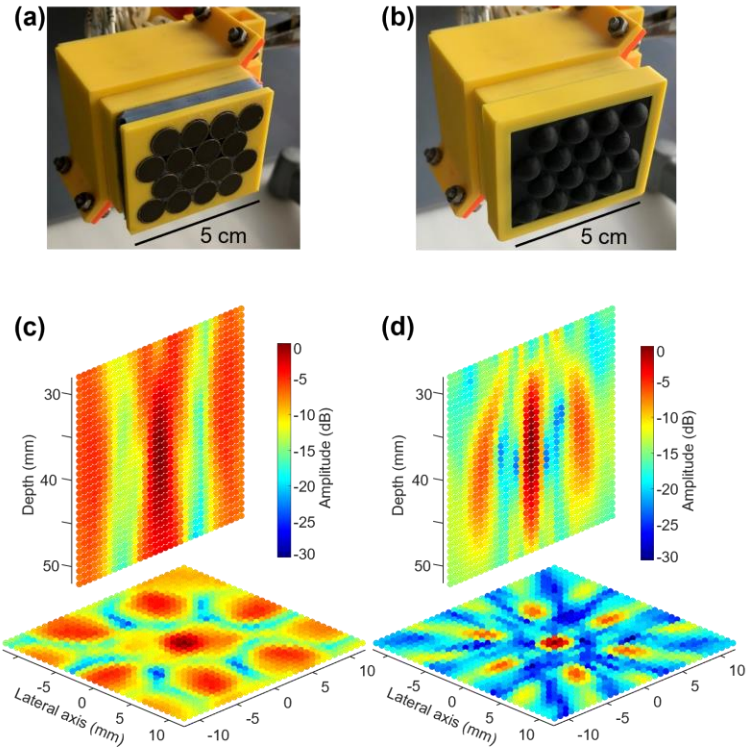

Figure 3. Transmit focusing study comparison of matrix array without/with lens. Photo of the matrix array composed of large elements of diameter 4λ without lens (a) and large elements of diameter 4λ with diverging lenses made of Stycast (b). Maximum pressure field in the axial and lateral planes, centred in the focal spot located at 4cm depth, corresponding to the 4λ matrix array (c), and 4λ matrix array with lenses (d).

3.2.2 Point spread function

The point spread functions (PSF) of the matrix array composed of large elements without and with lenses are compared in figure 4. The PSF at 4cm depth, corresponding to the matrix array composed of large elements without and with lenses are respectively shown in 3D figures 4 a) and 4 d), and the 2D maximum projection on the lateral plane figures 4 b) and 4 e) and the projection on the first lateral axis figures 4 c) and 4 f).

The 3 figures corresponding to the matrix without lenses 4a-c), show a poor PSF quality: the maximum of the image is not located at the location of the metallic tip [0,0,4cm] ±2mm, and grating lobes are superior to -2dB. When lenses are added the PSF quality is improved: the grating lobes' level is at -5dB and the main lobe corresponds to the maximum of the image which is located at the tip's position, with a 2,3mm width at -6dB.

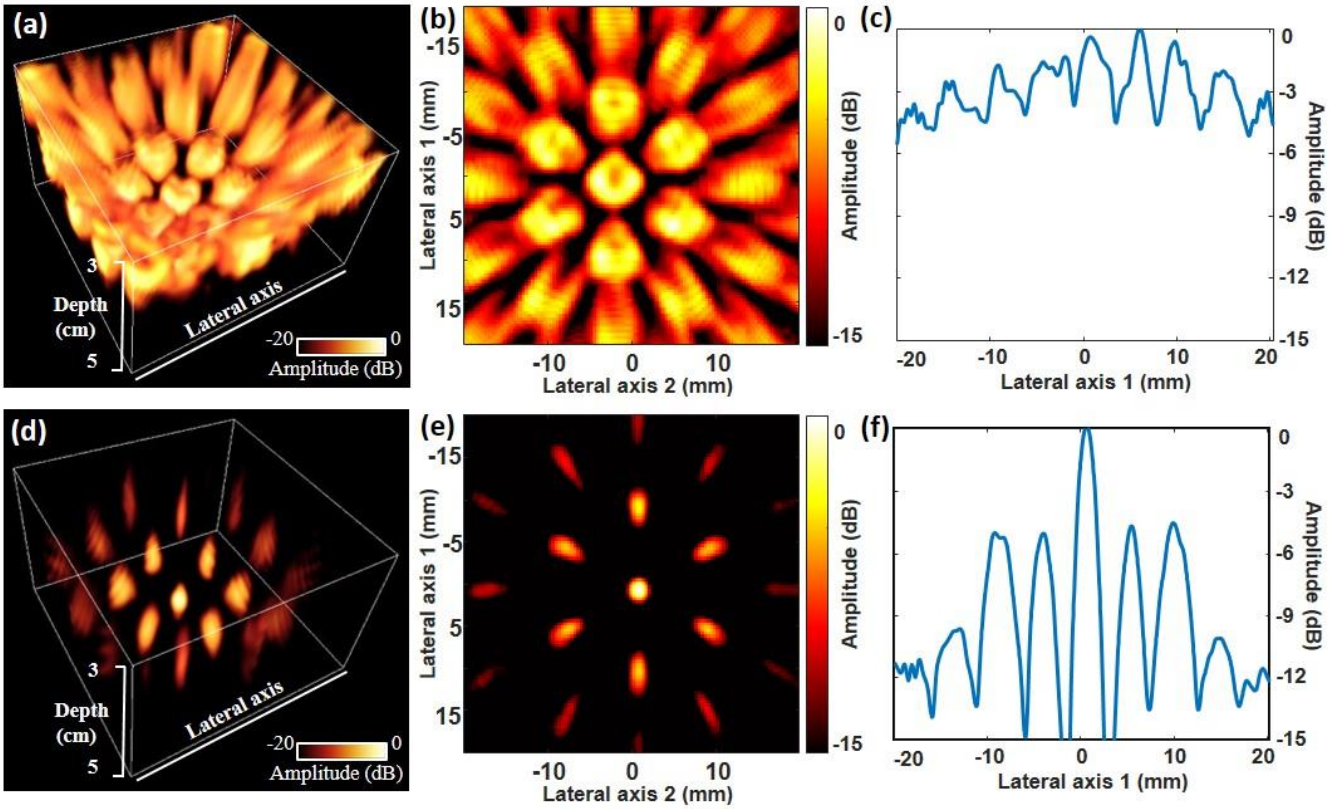

Figure 4. Point spread function (PSF) comparison, assessed at 4cm depth. a) 3D PSF obtained with the 4λ matrix array, (b) the maximum projection of the PSF in the lateral plane, and (c) the corresponding maximum projection amplitude profile on the 1st lateral axis. (d) 3D PSF obtained with the 4λ matrix array with the diverging lenses, (e) the maximum projection of the PSF in the lateral plane, and (f) the corresponding maximum projection amplitude profile on the 1st lateral axis.

3.3 Ultrasound localization microscopy: tube experiments

3.3.1 Tube imaging experiment imerged in water

ULM experiment had been carried out by imaging microbubbles flowing in tubes (1.5mm diameter) using the large element matrix array with the diverging lenses. Four frames spaced successively by 24 ms are displayed in figure 5 a) to show the image of two bubbles flowing in opposite directions. Two microbubbles, located in the tubes of opposite flow direction, are moving away from each other. The maximum projection of the frames on the lateral plane shows the hexagonal shape of the PSF seen previously in figure 4d-e).

The power doppler of the tubes is displayed in 3D figure 5b), which shows multiple complex helices structures duplicated due to the elevated grating lobes. After localization and tracking of the microbubbles, the grating lobes are filtered: the double helix is revealed on the density map figure 5c) and on the velocity map of the tubes figure 5d). 26 870 positions were localized and 18 871 locations were kept after tracking (ie. 70%). The velocity map figure 5d) is displayed in transparency and shows that absolute velocities close to the edge of the tube are lower than velocities near the center of the tube. This observation is confiremd by a perpendicular slice in 2D of the velocities figure 5d) upper right, and the velocities profile along the tubes cross section figure 5d) lower right.

The tube inner diameter as well as the absolute mean velocity were measured, 1.49mm (std=0.21mm) and 82mm/s (std=34mm/s) were found, which coresponds to a flow rate of 8.6ml/min. The flow rate found is consistent with the flow rate imposed of 6.7ml/min with the syringe driver.

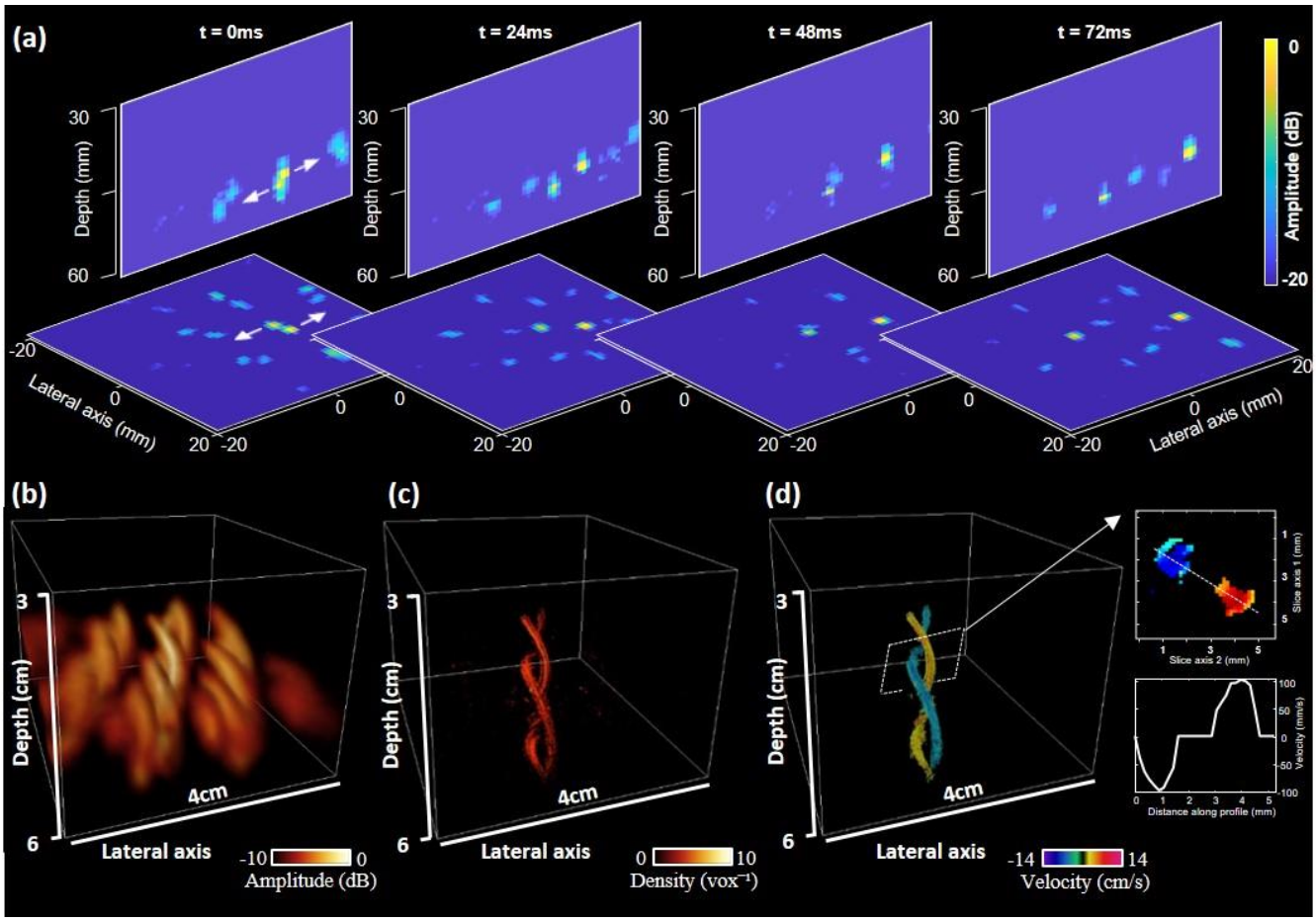

Figure 5. Ultrasound localization microscopy (ULM) of a tube using the 4λ matrix array with the diverging lenses. (a) Maximum projection in the axial plane and the lateral plane of four illustrative frames spaced by 24ms, showing two microbubbles circulating in the tubes of opposite flows, highlighted by the direction the white arrows. The power Doppler (b), density map (c) and velocity map (d), of the corresponding ULM experiment. A perpendicular slice is display (d) upper right, and the corresponding velocity profile along the dotted white line (d) lower right.

3.3.2 Tube imaging experiments through a human skull

A thin tube of 580µm diameter (λ/3), was imaged behind a human skull, using the large element matrix array with the diverging lenses. The experimental setup is shown in figure 6a). The PSF comparison without and with aberration correction is shown in figure 6b-c). The grating lobes' level decreases using aberration correction -3dB to -4.6dB.

The transcranial power doppler of the tube is shown in 3D figure 6d), the tube can be seen in the middle of the volume surrounded by six diffused lines up to -3dB corresponding to the grating lobes. The signal is maximum (0dB) at the center of the volume, where the tube is located. The transcranial density map obtained with the ULM technique is displayed in 3D figure 6e). 254 813 positions were localized and 88 292 locations were kept after tracking (ie. 35%). The tube appears clearly in the 3D volume, with a maximum density of 69 microbubbles detected in one voxel (150µm³). A maximum projection on the longest lateral axis is displayed figure e) upper right. The lateral length was found to be 32 mm. The inner diameter of the tube was measured, 571µm was found (std = 76µm) which corresponds to the inner diameter given by the manufacturer (580µm ± 80µm). Average velocity was measured, 77mm/s was found (std = 36mm/s), which corresponds to a flow rate of 1,2ml/min under the assumption of a Poiseuil flow distribution and using the measure of the tube diameter. The flow rate found is consistent with the flow rate imposed of 1ml/min with the syringe driver.

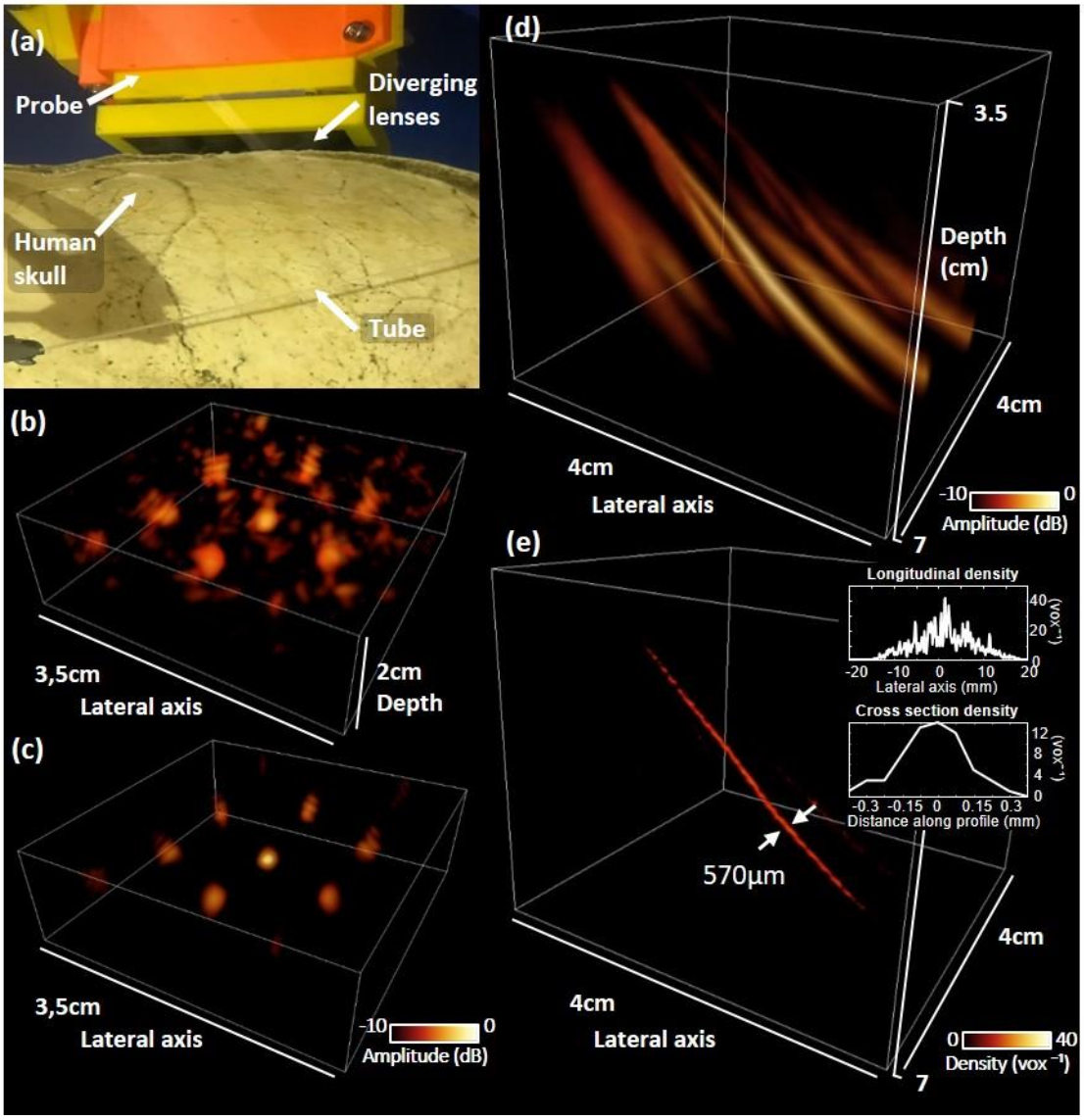

Figure 6. Transcranial ultrasound localization microscopy (ULM) of a tube using the 4λ matrix array with the diverging lenses. a) Photo of the experimental setup showing the 580µm diameter tube behind an adult human skull and the imaging system located near the temporal region of the skull. Transcranial point spread function at 5cm depth, without correction (b) and with aberration correction (c). d) 3D power Doppler and (e) the density map of the tube of the corresponding transcranial ULM experiment. Maximum projection on the longest lateral axis of the density map, and a density profile cross section of the tube are displayed e) upper right.

In vitro experiments were carried out to assess a more challenging transcranial ULM configuration (figure 7). Twisted 1.5mm diameter tubes of opposite flow were imaged behind the human skull. A picture of the experimental setup is shown in figure 7a). The transcranial ULM density map and velocity map are shown in 3D figure 7a) and b). N=74 365 positions were localized and N=20 880 locations were kept after tracking (ie. 28%). The velocity map (figure 7d) is displayed in transparency and shows that absolute velocities close to the edge of the tube are lower than velocities near the center of the tube similarly to the experiment in free space, figure 5c). The velocity cross section (figure 7c) upper right), and the velocity profile (figure 7c) lower right), show a Poiseuille profile. The tube inner diameter as well as the absolute mean velocity were measured, 1.55 mm (std = 0.18 mm) and 65 mm/s (std = 36 mm/s) were found, which corresponds to a flow rate of 7.5 ml/min. The measured flow rate was consistent with the imposed flow rate of 6.7 ml/min with the syringe driver.

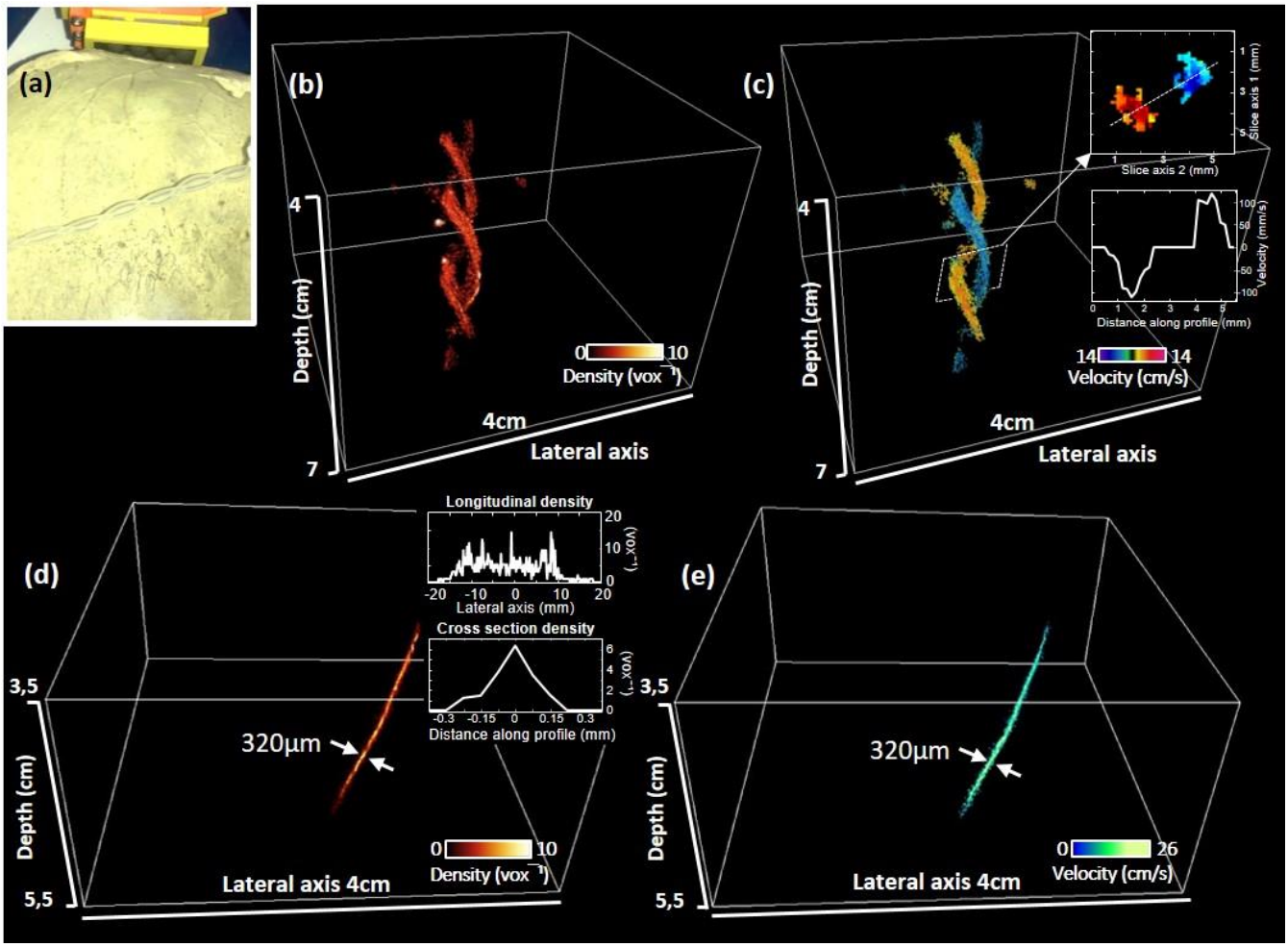

Figure 7. Transcranial ultrasound localization microscopy (ULM) of twisted tubes and sub-wavelength diameter tube (280 µm ie. λ/5), using the multi-lens array. a) Photo of the experimental setup showing the twisted 1.5 mm diameter tubes behind a human skull. Density map b) and velocity map c) of twisted tubes of opposite flow. A perpendicular slice is display (c) upper right, and the corresponding velocity profile along the dotted white line (c) lower right. Transcranial ULM Density map d) and velocity map e) of the 280 µm diameter tube. Maximum projection on the longest lateral axis of the density map, and a density profile cross section of the tube are displayed d) upper right.

A thinner tube of 280 µm inner diameter was imaged behind the human skull. The corresponding transcranial ULM density map and velocity map are shown respectively in figure 7d) and e). N=9128 positions were localized and N=4153 locations were kept after tracking (ie. 46%). A maximum projection on the longest lateral axis is displayed figure d) upper right. The tube lateral length was found to be 25 mm. The inner diameter as well as the absolute mean velocity were measured, 320 µm (std = 80 µm) and 167 mm/s (std=58 mm/s) were found respectively, which corresponds to a flow rate of 0.8 ml/min. The measure flow rate was consistent with the imposed flow rate of 0.5 ml/min with the syringe driver.

4. Discussion

In this study, we developed an ultrasonic array prototype made of large elements with diverging acoustic lenses for 3D large field ULM. The concept of multi-lens diffracting layer positioned in front of large piezoelectric elements was validated experimentally. The 4 by 4 element matrix array (41x31 mm) driven at low acoustic frequency was able to perform focusing in transmit-receive and image microbubbles to perform 3D ULM through an adult human skull bone.

Individual diverging acoustic lens in front of a large transducer (4.7λ diameter) maintains large angular aperture (up to 40° with lens compared to 12° without lens). It maximizes the transmit and receive energy. Acoustic pressure maps of focused transmits generated by a 4x4 matrix array composed of large elements, and large elements with lenses were measured in vitro

using a calibrated hydrophone. The matrix array composed of large elements with lenses was able to perform focusing at high acoustic pressure while maintaining lower grating lobes and better resolution compared to the matrix array without lens.

A twisted tube with two opposite flows was successfully imaged in 3D with the 16 elements matrix array with diverging lenses using an ultrafast transmit scheme. 3D ULM was performed to localize and track microbubbles previously injected. Density and velocity maps were obtained over a large field of view (4x4x3 cm^3) corresponding to the probe aperture. A Poiseuille velocity profile was observed, suggesting high precision of the proposed method. The probe high sensitivity was also demonstrated by imaging two sub-wavelength diameter tubes through a human skull immerged in a water tank. Inner diameter (580 µm ($\lambda/3$) and 280 µm ($\lambda/5$)) and flow rate (1 ml/min and 0.5ml/min) were retrieved. A twisted tube with two opposite flows was also successfully imaged behind the adult human skull bone.

Individual diverging lens combined with a large transducer increases the refraction angle of the incident beam while increasing the transducer sensitivity. It was first introduced in the photoacoustic field [20] to increase the acoustic signals received by the transducer. As sensitivity increased with the transducer surface, arrays of large transducers were developed to receive particularly weak photoacoustic signals. To increase the angular aperture of the large transducers individual acoustic lenses were placed in front of the transducers. Large angular aperture is requiered in the imaging field to perform focusing in receive and enable good image quality. As a comparison, transducers smaller than the acoustic wavelength classically used in ultraound imaging have a total angular aperture larger than 120°. Without lens, transducers larger than a few wavelengths have their angular aperture drastically reduced. With individual acoustic lens, large angular aperture can be restored using compound acoustic lens for instance. In the photoacoustic field, these particular arrays were only used in receive because light is the source of excitation. In this study, we extended the concept for the first time to transmit/receive ultrasound imaging to perform 3D ULM over a large field of view through the skull in vitro.

In our previous simulation study [22], large transducers with acoustic lenses were modelled as curved transducers in Field II simulation software. This simplified approach could demonstrate the potential of this technique by performing 3D ULM of a simulated vessel network. The use of a lens in front of a transducer is more complex than a curved transducer as it could involve a loss of acoustic signals due to absorption in the different materials and reflection at the interface of two materials due to acoustic impedance mismatch. In this study, the materials were not optimized to minimize these effects. Still, acoustic transmit pressure remained high, impulse response was not significantly affected by reflection and we were able to find similar results compared to the simulated curved transducers. No optimization on the lenses was done in this study except for the choice of Stycast material that has no impedance mismatch with water and limits reflections at this interface [28]. In the future, optimization of the materials will be performed to limit reflections at the interface between the piezoelectric material and the lens and to decrease absorption. To further increase the angular aperture, we introduced the compound lens which acts as a double diverging lens using the difference in the acoustic speed and the snell-descartes law for acoustic [24]. The curvature of the lens as well as lens material can be tuned to chose the directivity of the elements, depending on the application [29,30]. For transcranial imaging, the directivity of the element should not be too low otherwise it will spread the energy in a larger volume which may lower the sensitivity of the probe. Furthemore, the existence of the critical angle defined as the greatest angle of incidence for which an ultrasonic beam can strike the bone interface without being totally reflected could limit the interest of having the largest angle of incidence possible.

Large transducers provide large active surface with a reduced number of transducers. In this study, with only 16 transducers the probe surface covered a 31x41cm^2 area. At the edge of the probe, the bubble detection is more challenging due to the sensitivity drop off. The lateral field of view was approximately as large as the probe surface. To cover the same probe area to reach the same field of view with half-wavelength transducers, more than 1000 elements would have been needed. With our approach, the complexity in terms of probe wiring, transmit/receive electronic channels and associated cost was reduced by two orders of magnitude. To image the whole brain a larger probe's surface area (~100cm^2) will be needed. Using large elements, we expect that a few hundred of transducers could cover the entire brain. As a comparison, using small wavelength size transducers would require tens of hundred thousands of transducers that may not be sensitive enough to do transcranial imaging. Besides, it would require heavy technology developments and imply tremendous costs which would limit clinical translations.

Low transmit frequency (1MHz) was chosen to limit bone aberration and to image large volumes in term of imaging depth. If needed, we demonstrated the feasability of performing correction aberration to restore the point spread function quality. Such large volumes could enable whole cerebral vascular network imaging. Transcranial cerebral applications are envisioned but could be translated to cardiac or liver imaging for which imaging the entire organ through the bones is also challenging.

The ultrafast frame rate acquisition enabled the use of a high-performance singular value decomposition filter to distinguish moving bubbles from the tube walls. This aspect could be key to efficiently filter out tissue signal in an in vivo configuration.

Density maps can assess the vascular architecture and microbubble tracking can map the flow velocity and flow rate. These functional parameters could be crucial to help the diagnosis and monitoring of pathologies such as arteriovenous dysfunction diseases, intracranial aneurysms or stenosis, as well as the management of acute stroke.

Limitations include the large inter-element pitch creating high grating lobes compared to classical ultrasound imaging standards. In ultrasound imaging, grating lobes level must be as low as possible to ensure high B-mode imaging quality. However, in ULM techniques, it may not be crucial as individual microbubbles spatially separated are imaged and localized. This specificity enables to image with higher grating lobes level compared to B-mode imaging. In this study, the grating lobe levels are particularly high (up to -5dB at 4cm depth) and power Doppler volumes exhibit image replicates of the tubes. Still, the network of twisted tubes and the simple tube behind the skull were imaged and quantified precisely using 3D ULM. Localization and tracking algorithm was able to distinguish the signals from the main lobe and retreive microbubble location. High grating lobes level could be a limitation in presence of polydispersed population of bubbles. It could be difficult to separate the weak bubble signals from the grating lobes of the strong bubbles based on their amplitudes. However, in this study the distinction of main lobes from grating lobes was made possible by combining an amplitude threshold and a spatial correlation threshold. The spatial correlation treshold based on a gaussian PSF is key because grating lobes present an asymetric shape whereas the main lobes are more symmetrical (figure 4c-e). To enhance detection, the Gaussian PSF function could be replaced by the realistic PSF shape assessed experimentally or in simulation.

For in vivo applications, we may need to lower the level of grating lobes for real time postionning based on B-mode for instance. This could be achieved by reducing the inter-element pitch either by decreasing the diameter of the elements or the inter-element structure width (kerf), and by increasing the number of elements. In our case, the kerf accounts for 24% (2.2mm) of the inter-element pitch (9.2mm) due to metallic structures between individual elements. This inter-element structure can be lowered down to 100µm by probe manufacturer. In our previous simulation study [22], in which the inter-element was 6mm, the grating lobe level was -17dB for a PSF at 5cm depth. Breaking the periodicity of the element location, and optimizing the spatial distribution element could also be considered to further reduce the grating lobes [31,32].

The primary goal of this new ultrasound technology is to perform wide field of view ULM imaging of entire organs in 3D. In such configurations, the use of high-quality B-mode imaging for probe positioning could not be necessary. In clinical practice, positioning the probe to the right cross-section plane to evaluate relevant markers is crucial when using 2D ultrasound imaging. However, in the case of whole organ angiographic and hemodynamic imaging, the requirement for B-mode imaging is questionable as the relevant cross-section plane and markers could be assessed in post-processing. Nevertheless, lowering the grating lobes even more could be further needed if real-time B-mode imaging is explored. Synthetic aperture imaging [33] coupled to beamforming strategies such as adaptative beamforming by phase coherence [34] or short lag coherence of backscattered echoes [35] could be implemented.

Ultrasound is particularly sensitive to acoustic impedance mismatch and sound velocolity differences trough the skull, triggering attenuation and aberration. However, low transmit frequency (1MHz) limits the aberrations. Still, the SNR on transcranial images were enhanced by 2dB (see Figure 7b-c), by implementing aberration correction in post-processing. The aberrations were modeled as a near-field phase screen and were corrected by adding delays on each element of the matrix array as it is done in [8].

The skull attenuation could vary from one patient to another due to the thickness and/or porosity variations of the skull bone [36]. The SNR could further be increased in case of thicker skull using coded emissions with multiple transducers per transmit [37].

The imaging capabilities of the multi-lens probe were demonstrated in vitro, still, it needs to be proved in vivo. Indeed in vivo applications are more complex and safety measurements will be necessary for human applications. The robustness of the ULM method as well as maximal pressure measured in front of transducer (<1MPa, corresponding to a mechanical index of 1) are promising insight for furture works in which those points will be adressed. Moreover, to precisely assess the system resolution, one could conduct experiments with small tubes close to each other. In this study, we only demonstrated system feasibility but the precise resolution quantification will be addressed in future work with an optimized multi-lens probe.

Cerebral microvasculature architecture and dynamics assessments at the bedside of the patients would be a major improvement of patient care, as it addresses a major unmet clinical need. Ultrasound devices are portable, low cost, and non-ionizing and can map the hemodynamic at much higher resolutions than the current state-of-the-art MR and CT cerebral angiography. Microangiographic imaging could be of a major interest in the diagnostic of stroke and aneurysms as well as the monitoring of post-stroke recovery and aneurysms survey. For cancer, the 3D high-resolution mapping of gliomas could help to better define resection margins and improve surgical planning. It could also offer new insights into the fundamental understanding of complex lesions such as glioblastoma multiform and help monitoring tumour revascularization to enhance anti-angiogenic therapy outcomes.

The skull reduces the sensitivity when imaging with ultrasound due to absorption, multiple scattering and wave reflection. These characteristics limits imaging through small acoustic windows such as the temporal bone. These windows of a few centimeter squares limits the aperture size of the probes limiting resolution and sensitivity. Large element arrays with diverging lenses have the strong potential to alleviate current challeges in the ultrasound imaging field when imaging through the bones by proposing a new solution to image whole organs at high frame rates while maintaining a high sensitivity.

5. Conclusion

A new concept of matrix probe with large elements and diverging lenses for 3D large field ultrasound localization microscopy application was investigated in this article. An ultrasound 16 element matrix array prototype driven at 1MHz frequency was made and in vitro experiments were performed. The use of large elements enabled to increase the sensitivity and the aperture of the probe while maintaining a reduced number of elements. The diverging lens was shown to lower the directivity of the large element, which was essential to perform focusing and image reconstruction. The feasability of performing transcranial Ultrasound Localization Microscopy was validated by imaging sub-wavelength diameter tube (280µm) behind a human skull. The proposed multi-lens diverging layer has a strong potential for mapping whole organs 3D blood microcirculation while drastically reducing the elements count.

Acknowledgements

This work was supported by the AXA research fund and Inserm research accelerator (Inserm ART) in Biomedical Ultrasound. This work was also funded by European Union, European Research Council (ERC) grant agreement number 101042470. The GPU RTX A6000 used in this work was awarded by the NVIDIA Academic Hardware Grant Program.

References

[1] Portegies M L P, Koudstaal P J and Ikram M A 2016 Chapter 14 - Cerebrovascular disease *Handbook of Clinical Neurology* Neuroepidemiology vol 138, ed M J Aminoff, F Boller and D F Swaab (Elsevier) pp 239–61

[2] Couture O, Besson B, Montaldo G, Fink M and Tanter M 2011 Microbubble ultrasound super-localization imaging (MUSLI) *2011 IEEE International Ultrasonics Symposium* 2011 IEEE International Ultrasonics Symposium (IUS) (Orlando, FL, USA: IEEE) pp 1285–7

[3] Siepmann M, Schmitz G, Bzyl J, Palmowski M and Kiessling F 2011 Imaging tumor vascularity by tracing single microbubbles *2011 IEEE International Ultrasonics Symposium* 2011 IEEE International Ultrasonics Symposium (IUS) (Orlando, FL, USA: IEEE) pp 1906–9

[4] Viessmann O M, Eckersley R J, Christensen-Jeffries K, Tang M X and Dunsby C 2013 Acoustic super-resolution with ultrasound and microbubbles *Phys. Med. Biol.* **58** 6447–58

[5] Errico C, Pierre J, Pezet S, Desailly Y, Lenkei Z, Couture O and Tanter M 2015 Ultrafast ultrasound localization microscopy for deep super-resolution vascular imaging *Nature* **527** 499–502

[6] Foiret J, Zhang H, Ilovitsh T, Mahakian L, Tam S and Ferrara K W 2017 Ultrasound localization microscopy to image and assess microvasculature in a rat kidney *Sci Rep* **7** 13662

[7] Lin F, Shelton S E, Espíndola D, Rojas J D, Pinton G and Dayton P A 2017 3-D Ultrasound Localization Microscopy for Identifying Microvascular Morphology Features of Tumor Angiogenesis at a Resolution Beyond the Diffraction Limit of Conventional Ultrasound *Theranostics* **7** 196–204

[8] Demené C, Robin J, Dizeux A, Heiles B, Pernot M, Tanter M and Perren F 2021 Transcranial ultrafast ultrasound localization microscopy of brain vasculature in patients *Nature Biomedical Engineering* **5** 219–28

[9] Huang C, Zhang W, Gong P, Lok U-W, Tang S, Yin T, Zhang X, Zhu L, Sang M, Song P, Zheng R and Chen S 2021 Super-resolution ultrasound localization microscopy based on a high frame-rate clinical ultrasound scanner: an in-human feasibility study *Phys. Med. Biol.* **66** 08NT01

[10] Jensen J A, Holten-Lund H, Nilsson R T, Hansen M, Larsen U D, Domsten R P, Tomov B G, Stuart M B, Nikolov S I, Pihl M J, Yigang Du, Rasmussen J H and Rasmussen M F 2013 SARUS: A synthetic aperture real-time ultrasound system *IEEE Trans. Ultrason., Ferroelect., Freq. Contr.* **60** 1838–52

[11] Provost J, Papadacci C, Arango J E, Imbault M, Fink M, Gennisson J-L, Tanter M and Pernot M 2014 3D ultrafast ultrasound imaging *in vivo Phys. Med. Biol.* **59** L1–13

[12] Demeulenaere O, Bertolo A, Pezet S, Ialy-Radio N, Osmanski B, Papadacci C, Tanter M, Deffieux T and Pernot M 2022 In vivo whole brain microvascular imaging in mice using transcranial 3D Ultrasound Localization Microscopy *eBioMedicine* **79** 103995

[13] Demeulenaere O, Sandoval Z, Mateo P, Dizeux A, Villemain O, Gallet R, Ghaleh B, Deffieux T, Deméné C, Tanter M, Papadacci C and Pernot M 2022 Coronary Flow Assessment Using 3-Dimensional Ultrafast Ultrasound Localization Microscopy *JACC: Cardiovascular Imaging*

[14] Christensen-Jeffries K, Brown J, Aljabar P, Tang M, Dunsby C and Eckersley R J 2016 3-D In Vitro Acoustic Super-Resolution and Super-Resolved Velocity Mapping Using Microbubbles *IEEE Trans. Ultrason., Ferroelect., Freq. Contr.* **64** 1478–86

[15] Heiles B, Correia M, Hingot V, Pernot M, Provost J, Tanter M and Couture O 2019 Ultrafast 3D Ultrasound Localization Microscopy Using a 32x32 Matrix Array *IEEE Trans. Med. Imaging* **38** 2005–15

[16] Chavignon A, Heiles B, Hingot V, Orset C, Vivien D and Couture O 2021 3D Transcranial Ultrasound Localization Microscopy in the Rat Brain With a Multiplexed Matrix Probe *IEEE Transactions on Biomedical Engineering* **69** 2132–42

[17] Jensen J A, Ommen M L, Oygard S H, Schou M, Sams T, Stuart M B, Beers C, Thomsen E V, Larsen N B and Tomov B G 2020 Three-Dimensional Super-Resolution Imaging Using a Row–Column Array *IEEE Trans. Ultrason., Ferroelect., Freq. Contr.* **67** 538–46

[18] Wei L, Wahyulaksana G, Meijlink B, Ramalli A, Noothout E, Verweij M D, Boni E, Kooiman K, van der Steen A F W, Tortoli P, de Jong N and Vos H J 2021 High Frame Rate Volumetric Imaging of Microbubbles Using a Sparse Array and Spatial Coherence Beamforming *IEEE Trans. Ultrason., Ferroelect., Freq. Contr.* **68** 3069–81

[19] O'Reilly M A and Hynynen K 2013 A super-resolution ultrasound method for brain vascular mapping: Super-resolution ultrasound method for brain vascular mapping *Med. Phys.* **40** 110701

[20] Li C, Ku G and Wang L V 2008 Negative lens concept for photoacoustic tomography *Phys. Rev. E* **78** 021901

[21] Xia W, Piras D, Singh M K A, van Hespen J C G, van Leeuwen T G, Steenbergen W and Manohar S 2013 Design and evaluation of a laboratory prototype system for 3D photoacoustic full breast tomography *Biomed. Opt. Express* **4** 2555

[22] Favre H, Pernot M, Tanter M and Papadacci C 2022 Boosting transducer matrix sensitivity for 3D large field ultrasound localization microscopy using a multi-lens diffracting layer: a simulation study *Phys. Med. Biol.* **67** 085009

[23] Bamber J C 2005 Attenuation and Absorption *Physical Principles of Medical Ultrasonics* ed C R Hill, J C Bamber and G R ter Haar (Chichester, UK: John Wiley & Sons, Ltd) pp 93–166

[24] Yang S, Qin W, Guo H, Jin T, Huang N, He M and Xi L 2017 Design and evaluation of a compound acoustic lens for photoacoustic computed tomography *Biomed. Opt. Express* **8** 2756

[25] Jensen A J and Nikolov S I 2004 Directional synthetic aperture flow imaging *IEEE Trans. Ultrason., Ferroelect., Freq. Contr.* **51** 1107–18

[26] Papadacci C, Pernot M, Couade M, Fink M and Tanter M 2014 High Contrast Ultrafast Imaging of the Human Heart *IEEE Trans Ultrason Ferroelectr Freq Control* **61** 288–301

[27] Demene C, Deffieux T, Pernot M, Osmanski B-F, Biran V, Gennisson J-L, Sieu L-A, Bergel A, Franqui S, Correas J-M, Cohen I, Baud O and Tanter M 2015 Spatiotemporal Clutter Filtering of Ultrafast Ultrasound Data Highly Increases Doppler and fUltrasound Sensitivity *IEEE Transactions on Medical Imaging* **34** 2271–85

[28] Xia W, Piras D, van Hespen J C G, Steenbergen W and Manohar S 2013 A new acoustic lens material for large area detectors in photoacoustic breast tomography *Photoacoustics* **1** 9–18

[29] Bouzari H, Engholm M, Beers C, Stuart M B, Nikolov S I, Thomsen E V and Jensen J A 2018 Curvilinear 3-D Imaging Using Row–Column-Addressed 2-D Arrays With a Diverging Lens: Phantom Study *IEEE Transactions on Ultrasonics, Ferroelectrics, and Frequency Control* **65** 1182–92

[30] Engholm M, Beers C, Bouzari H, Jensen J A and Thomsen E V 2018 Increasing the field-of-view of row–column-addressed ultrasound transducers: implementation of a diverging compound lens *Ultrasonics* **88** 97–105

[31] Diarra B, Robini M, Tortoli P, Cachard C and Liebgott H 2013 Design of Optimal 2-D Nongrid Sparse Arrays for Medical Ultrasound *IEEE transactions on bio-medical engineering* **60**

[32] Ramalli A, Boni E, Savoia A S and Tortoli P 2015 Density-tapered spiral arrays for ultrasound 3-D imaging *IEEE Trans. Ultrason., Ferroelect., Freq. Contr.* **62** 1580–8

[33] Jensen J A, Nikolov S I, Gammelmark K L and Pedersen M H 2006 Synthetic aperture ultrasound imaging *Ultrasonics* **44** e5–15

[34] Camacho J and Fritsch C 2011 Phase coherence imaging of grained materials *IEEE Trans. Ultrason., Ferroelect., Freq. Contr.* **58** 1006–15

[35] Lediju M A, Trahey G E, Byram B C and Dahl J J 2011 Short-Lag Spatial Coherence of Backscattered Echoes: Imaging Characteristics *IEEE Trans Ultrason Ferroelectr Freq Control* **58** 1377–88

[36] Marsac L, Chauvet D, La Greca R, Boch A-L, Chaumoitre K, Tanter M and Aubry J-F 2017 *Ex vivo* optimisation of a heterogeneous speed of sound model of the human skull for non-invasive transcranial focused ultrasound at 1 MHz *International Journal of Hyperthermia* **33** 635–45

[37] Tiran E, Deffieux T, Correia M, Maresca D, Osmanski B-F, Sieu L-A, Bergel A, Cohen I, Pernot M and Tanter M 2015 Multiplane wave imaging increases signal-to-noise ratio in ultrafast ultrasound imaging *Phys. Med. Biol.* **60** 8549–66

ANNEXE 1: Lens material, acoustic properties characterization

Two plates of 6mm and 9mm width, made of the same batch material as the lenses (epoxy and silicone) were made to characterize its acoustic properties. The method followed is the one described in [28]. In a water tank at 22°C, ultrasonic signals of a transducer of the matrix array described in session 2.1.2, were acquired with the plates successively set next to the transducer surface. Acoustic signals were acquired thanks to a broadband needle hydrophone (HNC0400, Onda). The transducer and the hydrophone were distant by 30mm.

Acoustic signals from the two experiments with the different sample thicknesses were compared for each material. The difference in time-of-flight Δt and amplitude ΔA between of the experiment due to the different sample thickness Δd is used to compute the speed of sound in the material c, as well as the acoustic attenuation for our transducer temporal response (Eq2-3). The acoustical impedance of the material is also computed (Eq 4) from the speed of sound previously measured and the density ρ given by the manufacturer's technical data sheet. Measured acoustical properties of the material are gathered in Table 1.

The speed of sound measured experimentally were use in time delay laws, see Eq1., to beamform images.

$$c_{material} = \frac{c_{water}.\Delta d}{\Delta d - c_{water}.\Delta t} \tag{2}$$

$$\alpha_{material} = 20\log 10(\frac{\Delta A}{\Delta d}) + \alpha_{water} \tag{3}$$

$$Z_{material} = \rho.c \tag{4}$$

TABLE I

MATERIAL	Speed of sound (m/s)	Acoustic attenuation coefficient (dB/cm)	Acoustic impedance (MRayls)
Epoxy (Stycast1090SI)	2550	1.3	1.4
Silicone (Elite Double 8)	1000	1-2	1

Table1: Acoustic properties of the lens material